REPORT DOCUMENTATION PAGE

Form Approved
OMB No. 0704-0188

1. REPORT DATE *(DD-MM-YYYY)*	**2. REPORT TYPE**	**3. DATES COVERED** *(From - To)*
09/10/2012	Final	04/01/2009 to 03/31/2012

4. TITLE AND SUBTITLE

Magneto-Optic Devices Based on Organic Polymer Materials

5a. CONTRACT NUMBER

5b. GRANT NUMBER
FA9550-09-1-0192

5c. PROGRAM ELEMENT NUMBER

6. AUTHOR(S)
Nasser Peyghambarian
Robert A. Norwood

5d. PROJECT NUMBER

5e. TASK NUMBER

5f. WORK UNIT NUMBER

7. PERFORMING ORGANIZATION NAME(S) AND ADDRESS(ES)
Arizona Board of Regents
University of Arizona
888 N. Euclid Room 510
Tucson, AZ 85719

8. PERFORMING ORGANIZATION REPORT NUMBER

9. SPONSORING / MONITORING AGENCY NAME(S) AND ADDRESS(ES)
AFOSR
875 N. Randolph St., Rm. 3112
Arlington, VA 22203

Office of Naval Research
San Diego Regional Office
140 Sylvester Rd., Bldg. 140
Rm. 218
San Diego, CA 92106-3521

10. SPONSOR/MONITOR'S ACRONYM(S)
AFOSR/ONR

11. SPONSOR/MONITOR'S REPORT NUMBER(S)
AFRL-OSR-VA-TR-2012-1106

12. DISTRIBUTION / AVAILABILITY STATEMENT

~~XXXXXXXXXXXXXXX~~

Distribution A: Approved for Public Release

13. SUPPLEMENTARY NOTES

14. ABSTRACT The focus of this program has been to develop new magneto-optic (MO) composite polymer materials, including substituted polythiophenes, magnetic nanoparticles-polymer composites and other π-conjugated polymers with large MO Verdet constants to develop free space and integrable magneto-optic devices of interest to AFOSR. In this period a theoretical formalism has been established to suitably rationalize experimental Faraday rotation results from regioregular polyalkylthiophenes and their dependence on regioregularity. Magnetic nanoparticle core polymer shell nanocomposites have been modified with various surface functionalities to suit embedding in commercially available optical waveguide photoresists, such as SU-8 and the polysiloxane OE 4140 enabling a new set of polymer waveguide MO devices, a step closer to integrable isolators. A gadolinium based room temperature magnetic ionic liquid was developed with strong magneto-optic properties that is completely colorless and transparent up to 1.55•m enabling a capillary fiber based isolator device very similar to a 3mm long 65% Tb^{3+}-doped fiber isolator with 28dB isolation we have developed in collaboration with WPAFB. Collaborations with various Si-photonics groups have been established and works are underway to incorporate magnetic nanoparticles polymer composite materials developed under this program into Si-photonics platform for fabrication of compact, integrable isolators.

15. SUBJECT TERMS

16. SECURITY CLASSIFICATION OF:			**17. LIMITATION OF ABSTRACT**	**18. NUMBER OF PAGES**	**19a. NAME OF RESPONSIBLE PERSON**
a. REPORT	**b. ABSTRACT**	**c. THIS PAGE**			Nasser Peyghambarian
					19b. TELEPHONE NUMBER *(include area code)* 520-621-4649

Standard Form 298 (Rev. 8-98)
Prescribed by ANSI Std. Z39.18

FINAL PERFORMANCE REPORT

Abstract: The focus of the current program has been to develop new magneto-optic (MO) composite polymer materials, including substituted polythiophenes, magnetic nanoparticles – polymer composites, and other π-conjugated polymers with large MO Verdet constants to develop free space and integrable magneto-optic devices of interest to AFOSR.

Materials development: *Substituted polythiophenes:* A theoretical formalism has been developed to suitably rationalize our experimental Faraday rotation results from regioregular polyalkylthiophenes and their dependence on regioregularity. This work was performed in collaboration with Prof. Andre Persoons group at KU Leuven, Belgium. *MO polymer composites:* We have further extended our magnetic nanoparticle core polymer shell nanocomposites with modified surface functionalities to suit embedding in commercially available optical photoresists, such as SU-8 and polysiloxane OE 4140 enabling a new set of polymer waveguide MO devices, a step closer to integrable isolators. *Magnetic ionic liquids:* We developed a gadolinium based room temperature magnetic ionic liquid with strong magneto-optic properties that is completely colorless and transparent up to 1.55µm. A 2mm long broadband isolator fabricated using Polymicro™ capillary fiber filled with this liquid is currently under test.

Device development: *Tb^{3+}-doped fiber isolator:* Using a 3mm long 65% Tb-doped fiber we have developed a compact low magnetic field fiber based isolator (Faraday rotation of 45º at 0.35T) with ~28dB extinction. This work was carried out in collaboration with WPAFB. *All polymer waveguide devices:* Multiple sets of polymer waveguide Mach-Zehnder interferometers consisting of two polarization independent 3dB directional couplers have been developed for use with magnetite core-polymer shell nanocomposite as cladding. These devices are being tested for their MO waveguide performances. *Applications in Si photonics:* Currently collaborations are in place with Sandia National Laboratories and several European silicon photonics groups (University of East Finland, Technische Universitat Hamburg-Harburg).

Detailed report:

State-of-the art: The recent surge in demand for low cost integrated photonic components in the telecom and datacom industries has opened the door for novel technologies that enable unique functions and high yield manufacturing process. Advanced planar polymer technologies can fill the bill in every respect as shown by the recent surge in polymer-based integrated photonics component research and development, which has included Telcordia qualification of a number of polymer-based components. However, polymer waveguides with targeted MO applications are rarely found in the published literature and the state-of-the-art in this area is divided into two main categories (see Chart 1): traditional MO bulk materials based on the garnets that are not integrable, and the nanoparticle / polymer nanocomposites.

i) Garnet-based materials: In the near-infrared optical telecommunications regime magnetic garnet crystals are the only materials that combine high Faraday rotation with low optical losses. These materials have been the benchmark MO material for over 4 decades. The Faraday rotation of magnetic garnets can be strongly enhanced by the substitution of bismuth into the dodecahedral lattice sites of the crystals. Waveguides fabricated from the bismuth-substituted garnets (BIG) have been used to demonstrate MO isolators, magnetic field sensors and MO circulators. However, it has been difficult to incorporate BIG into semiconductor or Si-based PIC platforms due to the lack of physical or chemical bonding processes that can effectively couple light into the waveguides. Furthermore, due to a highly specialized crystal fabrication process, these materials are expensive. Numerous concepts have been designed and discussed theoretically, including polarization-independent devices using BIG based

waveguides. Up to now only a few of the theoretical models have been realized and tested experimentally. In this program we have developed a specialized laser writing system that enables fabrication of polarization independent polymer waveguides that are key to evaluating MO polymer materials for their waveguide MO performance. MO polymer nanocomposites (PNCs) inherently possess advantages for large-scale device integration, due to the ease of low cost fabrication and various possible means for integration with Si-based PICs. We note that demonstration of an MO PNC with equivalent MO performance to that of BIG (both Verdet constant and optical loss) in and of itself will have a ground-breaking influence on future integrated photonics research. This is reflected in the substantial commercial interest that our technology has already generated, with numerous inquiries from major optical component manufacturers such as JDS Uniphase (JDSU), Oz Optics, and Samsung.

Materials	Technology	Institute/ Company	Type	Performance	Status	Integrable to PIC platform
Substituted Garnets	Isolator	OZ Optics, Integrated-Photonics	Bulk	45° FR, > 20 dB Isolation, low loss	Fully developed	NO, Large, fiber coupled
	Sensor	Geophex Ltd	Bulk	100 pico Tesla /√Hz		NO, Large, fiber coupled
Electronic/ SQUID	Sensor	ARCOVA ELEKTA NeuroMag GEM	Bulk	10 femto Tesla /√Hz		NO, Large, operated at 4K
Gas	Sensor	Polatomic GEM	Bulk	300 femto Tesla /√Hz		NO, Large and Bulky
MO Polymer This program	Isolator	This group	Waveguide	> 2° FR, ~ 2 dB Isolation	Needs Development	Potential full integration
	Sensor		Bulk / Waveguide	10 pico Tesla /√Hz	Needs Development	Potential full integration

Chart 1: State-of-the-art and other research in MO materials and devices

ii) Polymer nanocomposites for optical applications: Recent synthetic advances in nanomaterials have enabled development of various nanoscale building blocks with distinct optical, electronic and magnetic properties. One of the important issues to be addressed for effective application in devices is how to systematically assemble these building blocks into an optically transparent processable material system. Whereas polymers have emerged as the prime candidate for the transparent passive host, various metal, metal oxide and semiconducting nanoparticles are being aggressively pursued for their potential applications in polymer based devices with unusual optical, electronic and mechanical properties. The interaction of light with these materials, which have fundamental working units much smaller than the light's wavelength, is particularly relevant considering the current drive to fabricate nanoscale photonic devices. This class of materials is commonly referred to as nanocomposites. The most commonly employed synthetic approach to forming such nanocomposites is the simple blending of polymers and nanoparticles, or *in-situ* polymerization in the presence of nanoparticles, but this method frequently

results in agglomeration and phase separation. An alternative strategy that has been explored in detail is based on loading the polymer matrix with metal ion precursors and synthesizing the nanoparticles *in-situ*. The polymer macromolecular matrix acts as a reaction chamber that provides a scaffold for immobilization, prevents aggregation and functions as a capping agent limiting and controlling nanoparticle growth. Charged polymers such as polyelectrolytes have been the primary choice for such approaches. Various metal oxide nanoparticles, including TiO_2, $CoFe_2O_3$, Fe_2O_3 and Fe_3O_4 have been synthesized within a polymer matrix by *in-situ* reduction / hydrolysis, to prepare nanocomposites with a wide range of properties.

At the outset of this program the regioregular polythiophene derivatives appeared to be potential candidate materials for their large Faraday rotation. However, at that time the origin of this effect in conjugated materials was poorly understood and in the last 3 years we have made great strides towards understanding a phenomenological relationship.

Magneto-optic and magnetic properties of regioregular polyalkylthiophenes: This section reviews work on the magneto-optical properties of π-conjugated polymers, in particular regioregular poly(3-alkyl)thiophenes. We give an overview of the theoretical formalism that led to the first observation of Faraday rotation from thin films of poly(3-dodecyl)thiophene and experimental results that include Faraday rotation studies from thin films composed of various polythiophene derivatives with varying degrees of regioregularity. We also discuss possible correlations between the Faraday rotation and the supramolecular organization within the thin films of these polymers. Magneto-optical properties, in particular Faraday (FR) rotation, were studied in thin films of various polythiophene derivatives. Faraday rotation is the rotation of the plane of polarization of linearly polarized light due to magnetic field induced circular birefringence of a material. In a non-absorbing or weakly absorbing medium a linearly polarized monochromatic light beam passing through the material along the direction of the applied magnetic field experiences circular birefringence, resulting in rotation of the plane of polarization. FR measurements are usually performed using AC and DC magnetic fields in a geometry with $\boldsymbol{k}$, $\mathbf{B} \,||\, \boldsymbol{z}$, where the FR angle is defined as $\theta = VBL = \pi \Delta n L/\lambda$ where Δn is the magnitude of circular birefringence (i.e. $n_{LCP} - n_{RCP}$) experienced by the medium under the applied magnetic field B, λ is the wavelength of light and L is the length of the medium. The constant V, the Verdet constant (expressed in degree/Tesla-meter, °/T-m) is a materials property and a quantitative measure of the FR ability of the material. The Verdet constant is strongly wavelength dependent, decreasing dramatically away from resonance and in the case of a paramagnetic material V also depends on the frequency of the magnetic field used.

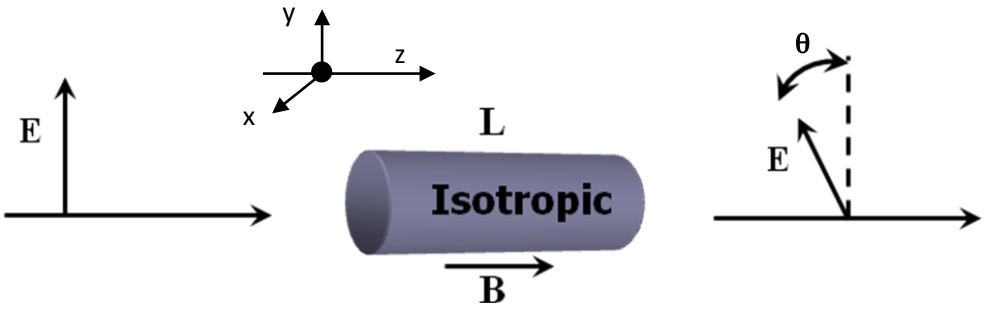

Figure 1. Experimental geometry for Faraday rotation measurements

We consider an experimental configuration for Faraday rotation measurements where a laser beam with frequency ω is transmitted through an isotropic sample under magnetic field B (Fig. 1). The electric field polarization inside the sample can be described as

$$P(\omega;\omega,0) = \chi_{xyz}^{eem}(\omega;\omega,0)E_y(\omega)\mathrm{B}_z(0)$$

and hence, $P_i = \chi_{ij}E_j + \chi_{ijk}^{eem}E_jB_k$ (1)

where $B(0)$ is the magnetic induction field and χ is the electric dipole allowed susceptibility, where the superscripts in the susceptibility components associate the respective subscripts with electric dipole (e) and magnetic dipole (m) interactions. Both linear polarization and magnetization act as sources for FR. Note that unlike χ^{eee}, χ^{eem} exists in all media, isotropic and anisotropic, indicating phenomenological similarity with Faraday rotation. (1) can be further reduced to

$$P = \chi^{B}E \text{ with } \chi^{\mathrm{B}} = \begin{pmatrix} \chi_{\mathrm{xx}} & \chi_{xyz}B \\ \chi_{yxz}B & \chi_{yy} \end{pmatrix} \quad (2)$$

Using symmetry arguments in the geometry described in Figure 1, one can derive $\chi_{xyz} = -\chi_{yxz} = \chi^{eem}$. Now Faraday rotation can be easily extracted as $\theta = VBL = \pi\frac{\Delta n}{\lambda}L = \left(\frac{4\pi^2}{n\lambda}i\chi^{eem}\right)BL.$ Using the χ^{eem} value of 0.4 pm/V reported earlier for the P3DT system, the Verdet constant V can be calculated to be 1.8×10^5 °/T-m, an encouragingly large number that certainly has been a major driving force in our research.

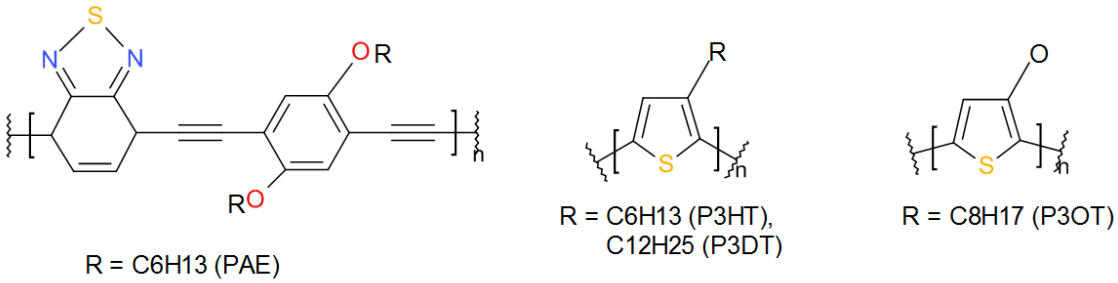

Figure 2. Molecular structures of the polymer systems

The molecular structures of the polymers studied in this project are given in Figure 2. The key candidates are poly(3-alkyl)thiophenes (PTs), poly(3-alkoxy)thiophenes (POTs) and poly(aryleneethynylene) (PAEs); the different chain lengths and regioregularity are also shown. Note that the PAE derivative is not an analogue to either of the polythiophene derivatives and was also first reported by a Japanese group subsequently verified by us. However, in the solid state of the PAE derivative the molecules are known to be self-assembled into a highly ordered face-to-face π-stacking structure, similar to regioregular PTs. In PAEs, π-interaction is considered to be stronger than in PTs and POTs, because of the higher planarity of the molecular backbone. PAE derivatives show larger FR than any of the PT derivatives studied so far. Table 1 lists wavelength dependent Verdet constants of the polymers studied. Within the PT derivatives FR measurements carried out on multiple spun coat films of RRP3DT, RRP3HT and their regiorandom counter parts show that the RR derivatives possess V on the order of 10^4 °/Tm as predicted from the χ^{eem} comparison. The regiorandom derivatives are either Faraday inactive or the rotation is below the detection limit of our system. Within measurement error both the polythiophene derivatives show quite similar Faraday activity and also depend strongly on the

crystallinity and the lamellae type structure of these polymers. When the spun coat films were subjected to different processing conditions followed by rigorous FR measurements, it was observed that the FR drastically decreased when the films were fabricated using melt processing. Details of the FR and x-ray diffraction studies of these thin films have been published by us previously. It was shown that the phase change above 80°C in the PT derivatives seems to be a critical factor influencing Faraday rotation indicating a strong dependence on processing conditions and interchain interaction, pointing towards the bound exciplex as the responsible moiety. On the other hand interchain charge transfer is known to be more robust in POT derivatives and we have previously observed that POTs show larger Faraday rotation than PT derivatives. It has been also shown that the FR from these materials is also a strong function of regioregularity. Poly(3-alkoxythiophene)s with different degrees of regioregularity were prepared using three different methodologies. It was shown that their FR is highly dependent on the degree of regioregularity, and FR was proposed to be a powerful technique to probe (small) variation in (supra)molecular structure of chiral as well as achiral conjugated polymers. Details of synthesis, characterization of purity, regioregularity and metal content estimation can be found in *Chemistry of Materials* **23**, 516 (2011).

Table 1. V, Verdet constant (10^4 degree/T-m) of polymers PAE, RRP3DT and RRP3HT at different wavelengths. Typically 200nm to 1μm films are used for these measurements. Standard deviations calculated from multiple independent measurements are shown in brackets. The values are also compared to Verdet constants of BK7 glass and that of a TGG crystal (⊥: values reported by others).

	532 nm	633 nm	670 nm	980 nm	1310 nm	1550 nm
PAE		25[⊥]				
RRP3DT	+ 2.06 (0.3)	+ 2.6 (0.6) 11.4⊥	+ 2.2 (0.2)	+ 1.6 (0.3)	+ 1.2 (0.2)	+ 0.85 (0.04)
RRP3HT (Spun coat)	+ 6.25 (0.3)	+ 4.42 (0.2) 20.3⊥	+ 4.02 (0.2)	+ 2.01 (0.04)	+ 1.04 (0.2)	+ 0.84 (0.03)
RRP3HT (Melt)	-	-	+ 0.60 (0.002)	+ 0.43 (0.003)	+ 0.21 (0.001)	-
BK7	+0.036	+0.025	+0.0223	+0.010	+0.0074	+0.0045
TGG[19]	-1.012	-0.813	-0.73	-0.34	-0.23	-0.15

Figure 3 shows the dependence of Verdet constant of P3HTs on regioregularity. The empirical fit indicates that the Verdet constant depends exponentially on the regioregularity. Note that such dependence is valid based on the assumption that the reported values of the regioregularity from the vendors are accurate within the measurement errors and the assumption that all samples had identical processing conditions. These observations further confirm that the FR in this class of conjugated polymers depends strongly on the supramolecular organization in their thin films. FR measurements on different π-conjugated polymers with varying degrees of band gap currently under study will be helpful in further elaborating the underlying mechanism.

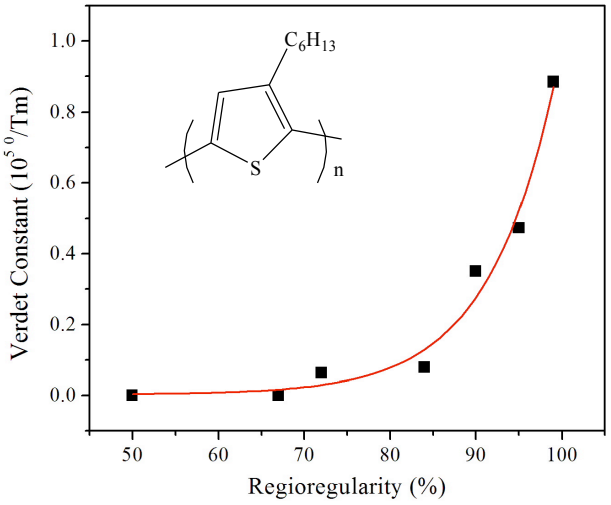

Figure 3. Verdet constant vs. regioregularity in RRP3HT thin films. Inset shows the structure of P3HT.

Magneto-optic properties of magnetic nanoparticles polymer composites: One of our major developments during this program has been the improved dispersion of nanoparticles in polymer composites. We have achieved this using our unique two-step approach that consists of (1) creating a polymer shell on the particle surface and (2) chemically linking the shell to the polymer host matrix. In this way we have been able to prepare Fe_3O_4 core - polymer shell nanoparticles dispersed in a polymethylmethacrylate (PMMA) matrix with little or no aggregation; unlike previously reported approaches, these composites have an appreciable degree of optical transparency in the visible and NIR region. The technique also enables us to chemically link the nanoparticles to the polymer host, enabling facile post processing of the polymer with minimal or no aggregation. One of the key advantages of this process is the ability to incorporate multiple polymer systems networked through the crosslinked particle core polymer shell nanocomposites, thereby allowing us to tune the refractive indices (RI) of the composite within a wide range. In a typical synthesis of cobalt ferrite particles polymer composites, 5mL of ethylene glycol (EG) and 25mL of hexafluorophosphate salt of 1-butyl-3-methylimidazolium (IL) were introduced into a 100mL round bottom flask and heated to 325°C. A mixture of EG and IL was used as the solvent. A solution of 2.7mg of $FeCl_3.6H_2O$ and 1.2mg of $CoCl_2.6H_2O$ in another 5mL of IL was injected into the hot solvent mixture. After refluxing for 6hr, the resulting brown solution was cooled down to 225°C and aged at that temperature for another 14hr. After aging, the mixture was cooled down and diluted with 100mL of deionized water. The entire solution was centrifuged at 8g and washed with deionized water repeatedly to remove excess ionic liquid. The particles were then dispersed in chloroform using oleyl amine. All chemicals were purchased from Sigma-Aldrich and were used as received without further purification.

Fig. 4 shows a transmission electron microscope (TEM) image of a collection of resultant nanoparticles with a mean diameter of 19.8 ± 0.24nm. Compositional analysis using energy dispersive X-ray spectroscopy shows a 1:2 atomic ratio of Co to Fe as expected. A high resolution TEM image of a single nanoaprticle shows the nearly single crystalline nature of the particles. The selected area electron diffraction (SAED) pattern collected on the particles could be readily indexed to cobalt ferrite particles. The rings in the SAED pattern also indicate averaging of the crystalline anisotropy within the sampled region, with the same crystal plane in different particles oriented randomly. The indexed SAED pattern indicates an inverse spinel type structure for the synthesized $CoFe_2O_4$ particles where oxygen atoms make up an FCC lattice and with one half of the Fe^{3+} ions occupying the tetrahedral A sites and the other half, together with Co^{2+} ions, located at the octahedral B sites.

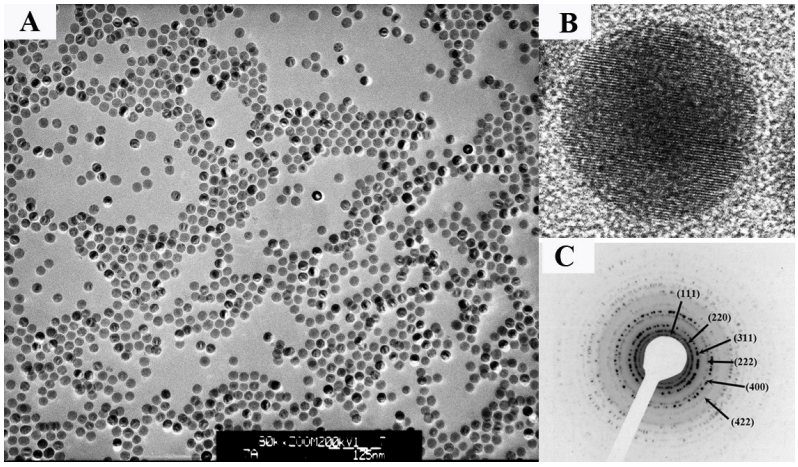

Figure 4. Transmission electron microscope image of a collection of cobalt ferrite nanoparticles (A), a high resolution image of a single nanoparticle showing the crystalline nature of the particles (B) and an SAED pattern of the nanoparticles indexed to cobalt ferrite crystals in (C).

We have previously shown a UV photoexcitation mediated polymer shell synthesis on magnetite nanoparticles. Using a similar methodology we have synthesized a polybenzylmethacrylate (PBMA) shell on the $CoFe_2O_4$ particle surfaces. In a typical synthesis, 10mg of particles, 0.2mL of benzylmethacrylate (BMA) in 10mL of chloroform was sonicated for 2hr at 60°C in a water bath before being illuminated with a 360-400nm photoexcitation source with nominal power of 10mW/cm^2. Photoexcitation is continued for 90min, during which the sonication and refluxing of the chloroform dispersion is continued. The reaction is monitored by following the vibration band of –C=C-H at 1628cm^{-1} using an FTIR spectrometer and once the band disappears the reaction mixture is cooled down to room temperature and subsequently the solvent volume is reduced to 2–3mL. Figure 5 shows a scanning TEM image of the $CoFe_2O_4$ particles core PBMA shells with ~4nm thick shells. Under TEM, a few particles were seen to form a chain (shown as inset in Figure 5) which is expected given the fact that $CoFe_2O_4$ is known to acquire ferromagnetic properties in particles with diameter >20nm which is close to the

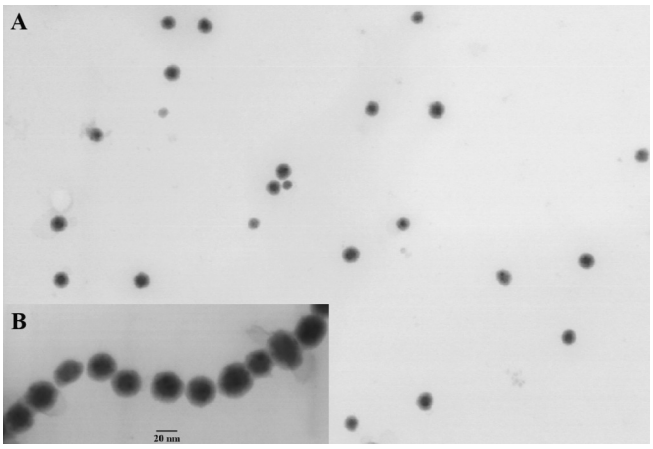

Figure 5. STEM image of the $CoFe_2O_4$ particle core PBMA shell composites in A. Inset: Higher magnification STEM images of the composite particles forming a chain.

particle sizes obtained here. However, in DC FR measurements reported below, we have not observed any hysteresis, indicating that the ferromagnetic $CoFe_2O_4$ particles, if any, are small in number and below the sensitivity level of our Faraday rotation measurement setup. The detailed characterization and reaction rate of this shell formation process has been discussed previously in *Nonlinear Optics and Quantum Optics*, **41**, 87-104 (2010). To further probe the nature of this reaction, we carried out high resolution X-ray photoelectron spectroscopy (XPS) on a representative magnetite nanoparticles-BMA shell composite system. A monolayer of magnetite nanoparticles was created on top of perfluorosilanized SiO on a silicon substrate using a self-assembly technique. This assembly of particles was dipped into a BMA/chloroform solution and was then illuminated with a 400nm photoexcitation source. XPS spectra were recorded on the samples before and after the photoexcitation as shown in Fig. 6. The C1s XPS peak at 283.4eV and the O1s doublet at 529eV indicate new Fe-C and Fe-O bond formation after photoexcitation of the particles. $CoFe_2O_4$ particles are expected to follow a similar reaction pathway. The shell formation on top of the particles helps prevent aggregation among particles and improves long term stability and optical quality of the composite.

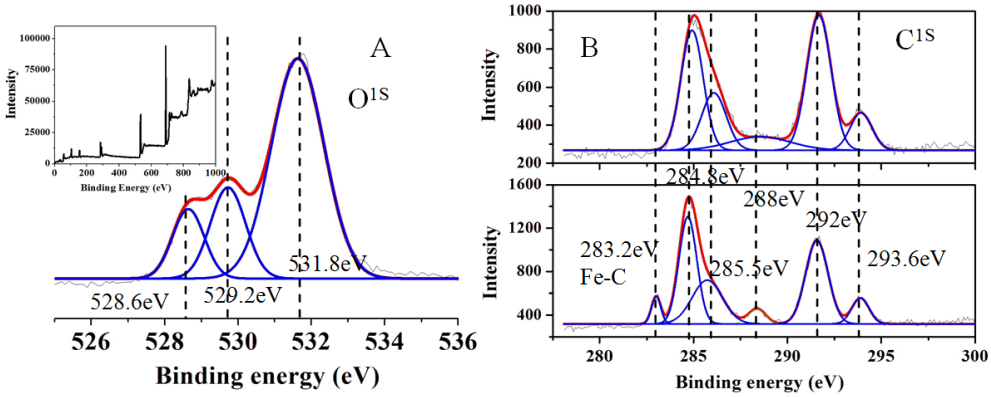

Figure 6. XPS results for Fe_3O_4 nanoparticles: A. High resolution O1s spectra shows a 3 component XPS spectra of Fe-O bond, the splitting of the O1s at 530eV indicates new Fe-O bond formation after photoexcitation; B. Fe_3O_4 BMA mixture before (top) and after (bottom) PBMA shell formation, the new C1s peak at 283.2eV indicates possible Fe-C bond formation due to photoexcitation.

Figure 7 shows a representative plot of refractive indices of 15 nm magnetite nanoparticles with (polybenzylmethacrylate) PBMA shell dispersed in a PMMA-PBMA-TMPT crosslinked matrix. Whereas at fixed nanoparticle concentration, the resultant refractive index appears to be a weighted linear

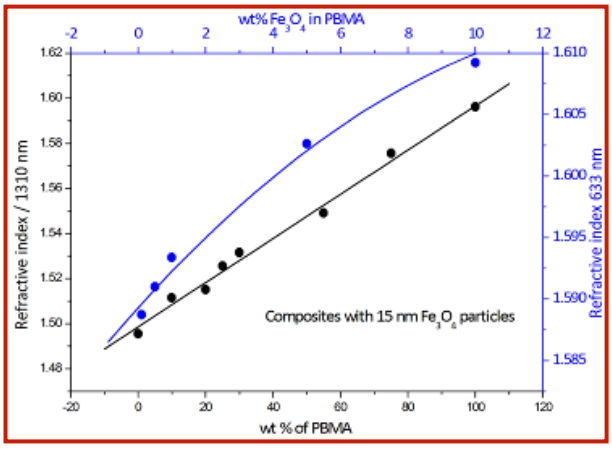

Figure 7. RI of Fe_3O_4 PBMA composite vs. the wt% of PBMA (black) and that of the particles (blue).

combination of the RIs of the component monomers (data shown at 1310 nm), in a single polymer matrix, such as, PBMA, the RI of the composite follows Maxwell Garnet volumetric dependence on the nanoparticles. We have also reported that these composites show MO rotation that is comparable to some of the commercially available garnets. Furthermore, we have shown that MO activity from these composites is strong function of:

i) *Particle size:* FR in magnetite (Fe_3O_4) PMMA composites follows the general relation $\theta_F = \theta_F^t \left[1 - 3\left(\frac{2t}{d}\right) + 3\left(\frac{2t}{d}\right)^2 - \left(\frac{2t}{d}\right)^3\right]$ where θ_F^t is the size dependent FR, and t is the non-crystalline dead layer on the surface of a particle with diameter, d. However, note that increasing the size of the particles may increase the optical scattering along with the FR. Magnetite nanoparticles with diameter of 18nm shows $\theta_F^t \approx$ 210°/cm in 5wt% composite in PMMA with minimal scattering and high transparency.

ii) *Wavelength dependence:* FR is generally an absorption mediated process and is strongly dependent on the wavelength of measurement. Figure 8 gives a comparison of the wavelength dependent Verdet constants for the composites **A**, **B**, **C** and **D**. Within the wavelength range investigated, the FR magnitude and sign of **A**, **C** and **D** are comparable, with a saturation field between 50 and 60mT. We interpret this similarity to arise from the dominant effects of the Fe_3O_4 interband transitions on the diagonal and off-diagonal terms of the MO tensor in the absorptive region. Composite D shows the maximum Faraday rotation at 980 nm. A detailed description of origin and MO performance has been reported in *Applied Physics Letters* **95**, 143302 (2009).

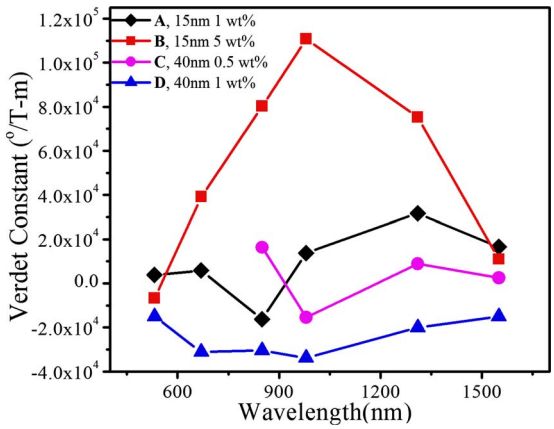

Figure 8. Wavelength dependence of the Verdet constants of A, B, C and D (see plot for wt% composition). Solid lines are guides to the eye.

Table 2 gives a comparison of Verdet constants at different wavelengths of two representative ferrite-based PNCs prepared with 15 nm Fe_3O_4, and 10 nm $Dy_xCo_{(1-x)}Fe_2O_4$ particles. An array of spinel ferrite nanoparticles, MFe_2O_4 (M = Mn, Mg, Zn, Co, Ni, Cu, Fe etc.) can be developed; these materials have complex magnetic couplings at their two types of cation occupying lattice sites (A and B). Due to the high compositional and structural flexibility, spinel ferrite nanoparticles offer great opportunities for designing and fine-tuning the magnetic properties of nanoparticles. By using magnetic cations with appreciable spin-orbital coupling strength, such as the case of Dy doping, the onset temperature of superparamagnetic transition can be controlled. By adjusting the magnetic cation distributions at the A and B lattice sites, the saturation magnetization can be maximized. Development of these particle systems has been a priority under this program and we have made significant progress.

Table 2. A comparison of wavelength dependent Verdet constants of 2 representative PNCs

Verdet constant (10^4 °/T-m)	980 nm	1310 nm	1550 nm
Fe_3O_4 NP polymer composite	11.5	7.8	2.0
$CoDyFe_2O_4$ NP polymer composite	62.6	10.6	9.2

Magnetic field poling: Recently we have shown that magnetic nanoparticle assemblies embedded in a polymer host can be potentially useful as active elements in various MO applications due to their enhanced FR compared to their native state. Conventional methods of constructing 1D nanoparticle arrays consist of top-down methods like lithographic techniques or the electro-deposition of materials into linear pores. Bottoms-up strategies usually involve the manipulation of linear templates. Externally applied magnetic fields have also been utilized to align magnetic nanoparticles into 1D and 2D arrays. These processes can be either procedurally cumbersome or may require sophisticated equipment and expensive precursor materials. The use of linear magnetic particle assemblies in device applications, however, necessitates their large-scale production. This requires a production method that is robust and inexpensive but simple in design. We have now developed an inexpensive and simple method of producing 1D magnetic nanoparticle arrays embedded in polymer host, which display orientation-dependent MO characteristics due to their assembled morphology (see Figure 9), via a novel magnetic field poling process.

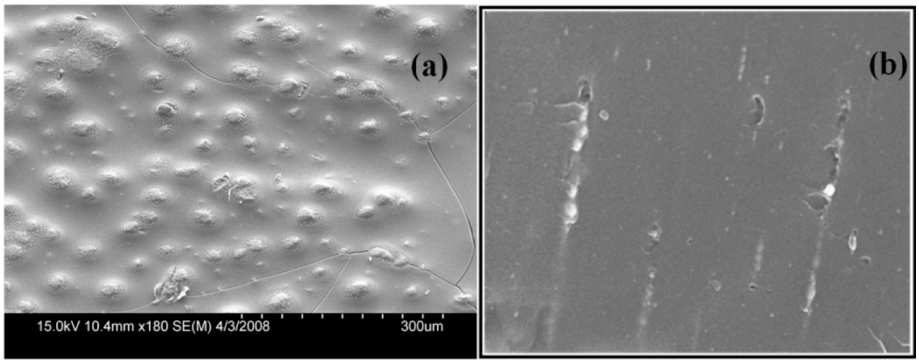

Figure 9. (a) SEM image of top surface of a magnetic field poled MagC-PBzMA in PMMA nanocomposites. (b) SEM cross-section of a poled composite, with the induced magnetic anisotropy axis at 80º with respect to sample plane.

Figure 10 shows a comparison of measured Faraday rotations under dc magnetic field before and after magnetic field poling. The magnetization curves of the poled (aligned) sample show a clear influence of the alignment field. The coercive fields and the normalized remanence are significantly higher than those in the pristine sample. However, the saturation FR of the pristine film is expected to rise further and possibly match that of the poled film, albeit at much higher applied magnetic field; considering a statistical

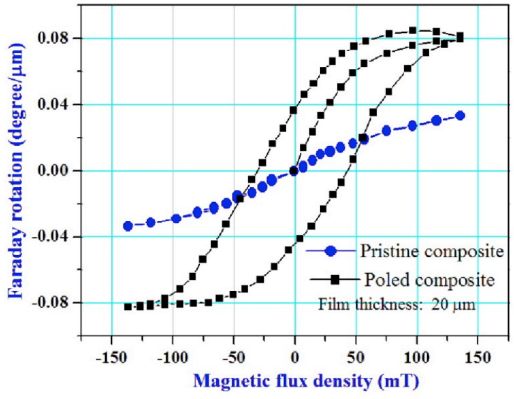

Figure 10. Comparison of FR measured using dc applied magnetic field for poled and pristine composites.

volumetric average of the interacting particles that influence light polarization, the total magnetization is the same in both poled and pristine samples. Note that this is an entirely new approach for fabricating polymer based MO active materials with high transparency as well as residual (remnant) MO Faraday rotation at room temperature. It is our hypothesis that by fine-tuning magnetic field poling conditions a magnetic polymer nanocomposite material can be fabricated that not only possesses a large Verdet constant but also is highly transparent at the wavelength of interest. We have also developed a cobalt nanoparticles based composites with unique core-shell architecture and ferromagnetic properties. For efficient room temperature operation of MO isolators, PNCs incorporating ferromagnetic nanoparticles will be best with the primary benefit that devices based on them will not require a permanent magnet. This is a significant advantage over traditional isolator MO materials and the superparamagnetic PNCs previously developed by us. For example Figure 11 shows FR measurements on two different types of PNCs, a) ferromagnetic cobalt (Co) nanoparticles (30 nm diameter) polystyrene (PS) based PNC, and b) superparamagnetic magnetite (Fe_3O_4) nanoparticles (15 nm diameter) polymethylmethacrylate (PMMA) based PNC, both developed by the UA team. The FR response of the PNCs follows the magnetization of the constituent nanoparticles. DC FR was measured using a polarization modulation scheme coupled with an MO polarimeter. The measured coercivity using FR, ~2000 Oe is similar to the reported value for Co particles of comparable size [J. Pyun et. al., *ACS Nano* **3**, 3143 (2009)]. Reported saturation magnetization of Co particles of 30 nm diameter is on the order of 40emu/g. For PNCs with 5wt% Co particles the saturation magnetization scales to 2emu/g of PNC. In Figure 11 the FR data shows a ~0.5° of rotation at zero applied field from a 15μm thick sample. There is potential for new materials based on this strategy with magnetization expected to be on the order of 1000 emu/g allowing us to use 50μm long waveguide devices as an isolator. The slight asymmetry in the DC FR plot at zero applied magnetic field is most likely due to different capacitive loads in the solenoid for positive and negative magnetic field.

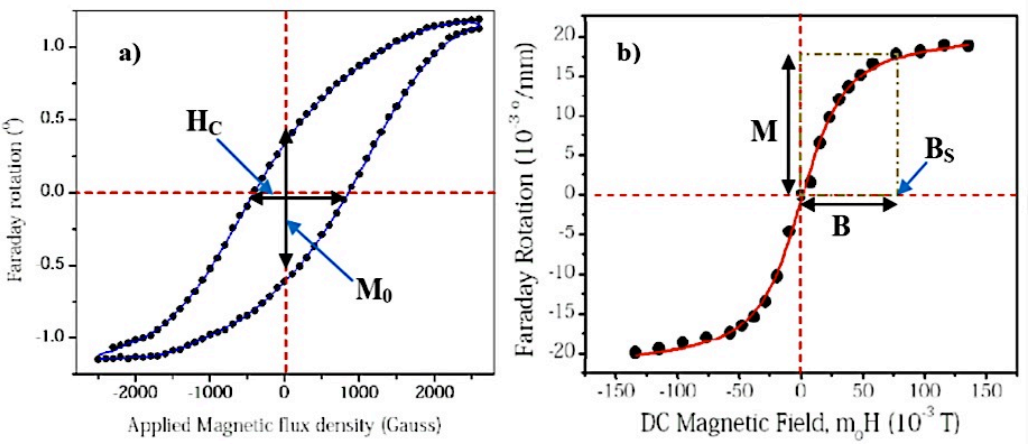

Figure 11. FR from a) CoPs and b) Fe_3O_4 PMMA PNCs

For MO isolator and circulator applications, our goal is to maximize H_C (coercivity) and M_0 (residual magnetization) in ferromagnetic particles. The goal here is to increase the loading of the ferromagnetic nanoparticles with large H_C and M_0 in order to improve the FR of the material where $\theta \propto M_0$. A large value of M_0 (on the order of 1000 emu/g) will significantly reduce fabrication costs and steps as the device fabricated will not require an external magnetic field; also a large H_C will provide a robust magnetic system with long-term stability of its magnetic properties. The particles and the polymer matrix should not only be compatible to avoid species segregation and crystallization of the material, but also must be prevented from aggregating during post processing. The preparation of ferromagnetic

nanoparticles based on metallic cobalt, FeCo alloys and FePt bimetallic phases has been accomplished under this program. Using *in-situ* methods, PS-CoNPs over a range of size from 15-50 nm have been be synthesized, while maintaining uniform size distributions as shown in Figure 12. The magnetic moment and coercivity of these PS-CoNPs directly scales with particle size enabling access to a range of magnetic moments (30-100emu/g) and coercivity (200-1200Oe), respectively, at room temperature. PS-CoNP PNCs with particle sizes of 22.5nm, 27.4nm and 43nm have been tested. We have also used our magnetic field poling technique to align the PSCoNPs to enhance FR and the figure of merit, where we have achieved a factor of eight improvement in FR using magnetic field poling.

The saturation FR (in °) and FOM (in °) of the present PS-CoNP PNC is compared to those of Fe_3O_4 PMMA superparamagnetic PNC, along with commercially available bismuth substituted garnets (BIG) in Table 3. Alignment of nanoparticles increases the transparency and hence there is an increase in FOM in the magnetic field poled samples. Although input polarization dependent, magnetic field poling increases FR and FOM in all PNCs.

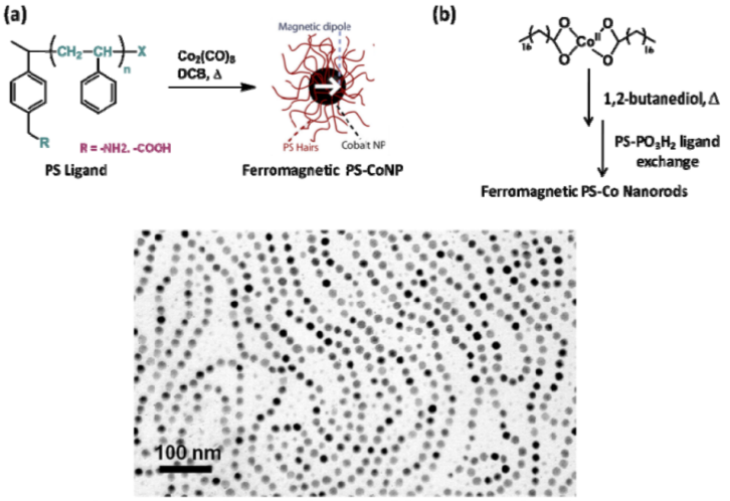

Figure 12. Synthesis and TEM of ferromagnetic PS-CoNPs

Table 3. Optical and MO properties of different nanoparticles and polymer composites.

Composition	sp Diameter (nm)	Ms [A/m] 300K	Ferromagnetic diameter (nm)	Refractive index (n_D)	Specific FR of composite At 1550nm
Fe	3.0 – 9.3	10^5 - 10^6	>12	2.0 – 2.3	N/A
Co	2.0 - 12	10^4 - 10^5	>18	2.80	320°/cm 2150°/cm (poled)
Fe_3O_4	8.0 - 30	4.8 – 5.2 x 10^5	>40	2.42	350°/cm 800°/cm (poled)
$CoFe_2O_4$	2.0 - 12	8 x 10^4	>20	2.23	10°/cm
Bi-YIG	N/A	N/A	N/A	3.47	12857°/cm

Applications in magnetic field sensors: The nearly monodisperse distribution of the nanoparticles shown in the TEM and STEM images shown above is an indication of the expected optical quality of the $CoFe_2O_4$ nanocomposite, as scattering is directly related to the amount of clustering and nanoparticle aggregation. The nanocomposite as a whole was uniform and showed excellent optical transmission. The nanoparticle content of the $CoFe_2O_4$ nanocomposite was 4wt% as determined by thermogravimetric analysis. Fig. 13 shows the absorption spectra of the $CoFe_2O_4$ nanocomposite, and Fig. 13a and Fig 13b show a 170 μm thick film over a computer LCD display and a 100μm thick film with a 1 inch diameter directed at the street, showing details of both the screen pixels and of distant objects with excellent optical quality, respectively. Table 4 gives the Verdet constant values at 850nm, 980nm, 1310nm and 1550nm. The saturation Faraday rotation at 980nm was 0.0011 °/μm and was measured using a single pass DC MO polarimeter with a Hinds Instruments photoelastic modulator PEM-100 to enable phase locked detection; calibration was performed with a two pass AC MO homodyne polarimetric configuration used for the Verdet constant measurement of a 75μm thick film of $CoFe_2O_4$ nanocomposite, shown in the Fig. 14 inset. The data shown in Fig. 14 was fitted with a modified Langevin shape previously used in for this type of magnetic core polymer shell nanocomposite and the correlation factor was R^2=0.996. The figure of merit at 980nm is 0.95° (FOM = $2\theta_F^S/\alpha$) which is comparable to the yttrium iron garnet FOM of 4.2° at the same wavelength. The high Verdet constant values and low absorption, particularly at 1550nm, make the $CoFe_2O_4$ nanocomposite an interesting alternative to the 5wt% magnetite nanocomposite, as the ratio V/α of the $CoFe_2O_4$ nanocomposite is an order of magnitude higher at 1550nm.

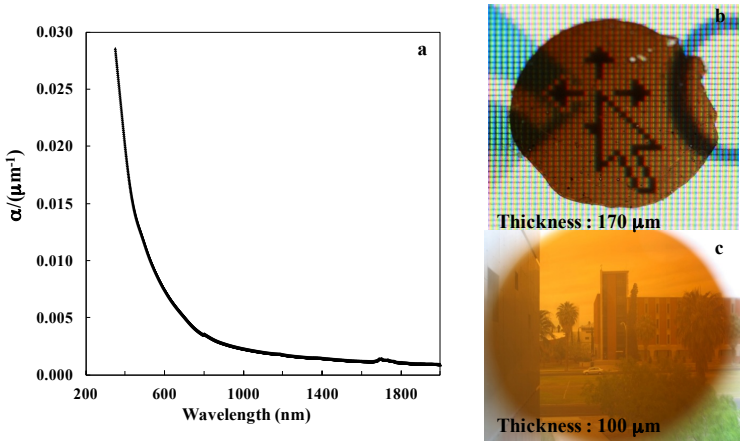

Figure 13. Absorption spectra of 4wt% $CoFe_2O_4$ nanocomposite (a), transmission of a 170μm thick film on a LCD display (b), and street view transmission of a 100μm thick film(c).

Table 4. Verdet constant values of the 4 wt% $CoFe_2O_4$ nanocomposite at different wavelengths**.**

	850 nm	980nm	1310nm	1550nm
Verdet constant (°/T-m)	-1.9×10^4	-1.2×10^4	-2.2×10^3	-1.5×10^4

The 170μm free standing film shown in Fig. 13b was used a sensor head MO element. The film was prepared by melt processing and subsequently attached to a gold-coated mirror on a 250μm thick glass substrate. The nanocomposite sensitivity was tested in the optical configuration shown in Fig. 15c with a 980nm laser. The sensing head also consisted of two tapered cylindrical magnetic flux concentrators made of Ferroxcube 3B1 MnZn ferrite materials, with an initial permeability of 900 at room

temperature. The introduction of high magnetic permeability materials such as MnZn ferrite has been used to enhance the magnetic flux density at the sensing MO element. The glass substrate was fixed to a solid tapered magnetic flux concentrator of 3B1 and a hollowed out concentrator that allows access for the optical probe was fixed to the exposed polymer surface. The outer diameter of the concentrators was 10mm and was tapered to 4mm and 2mm for the front and back concentrators, respectively, at a 45° angle. Fig. 15b shows the assembly of the concentrators and the MO sensing element, where the front concentrator has a clear aperture of 2mm diameter. The high permeability of the concentrators enhances the magnetic flux density at the smallest diameter of the solid concentrator and channels to the front hollowed concentrator as it propagates through the MO nanocomposite film. Fig. 15a shows the distribution of the magnetic flux density component parallel to the propagation vector **k** as simulated in COMSOL. The otherwise uniform magnetic field generated by the Helmholtz coil is sharply increased at the front of the solid concentrator, especially at the edges of the taper as this is the closest path to the front concentrator.

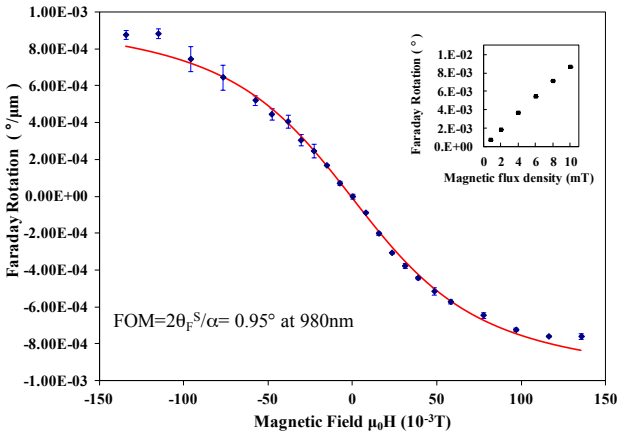

Figure 14. Faraday rotation of $CoFe_2O_4$ nanocomposite at 980nm, inset: AC Faraday rotation for Verdet constant measurement at 980nm.

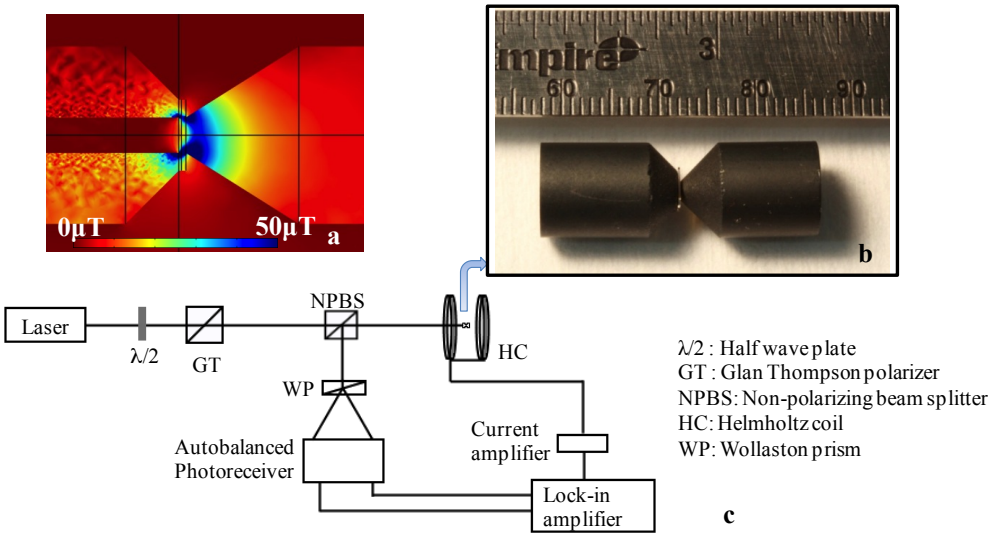

Fig. 15. Magnetic flux density distribution in the vicinity of the MO polymer film (a), probe photograph showing the assembly of concentrators and MO film (b) and optical configuration schematic (c).

The sensitivity was measured with a 3μT 500 Hz control magnetic field generated by a Helmholtz coil. The magnetic field was measured with a commercial gaussmeter Hall probe. Fig. 16 shows the sensitivity, signal to noise ratio (SNR), and minimum detectable field B_{min} of the magnetometer at various measurement time constants. Point-to-point comparison of the sensitivity indicates that the magnetometer has noise equivalent magnetic field sensitivity of ~50nT/√Hz as seen by the red dashed line in Fig. 16. Using magnetic flux concentrators, the sensitivity of the sensor is enhanced by roughly a factor of 20 (red solid line) compared to the probe without a concentrator surrounding the polymer nanocomposite. The sensitivity, SNR and B_{min} in the absence of magnetic flux concentrators is shown in dashed lines in Fig. 16. The sensitivity can be further improved by taking advantage of the low scattering of the MO polymer, using a thicker film, employing magnetic field poling to increase the MO response of the nanocomposite, as well as exploring other nanoparticle systems with a higher magnetic permeability, as one of the most important factors that drive the magnetic field concentration is the contrast of magnetic permeability between the concentrators and the MO nanocomposite film.

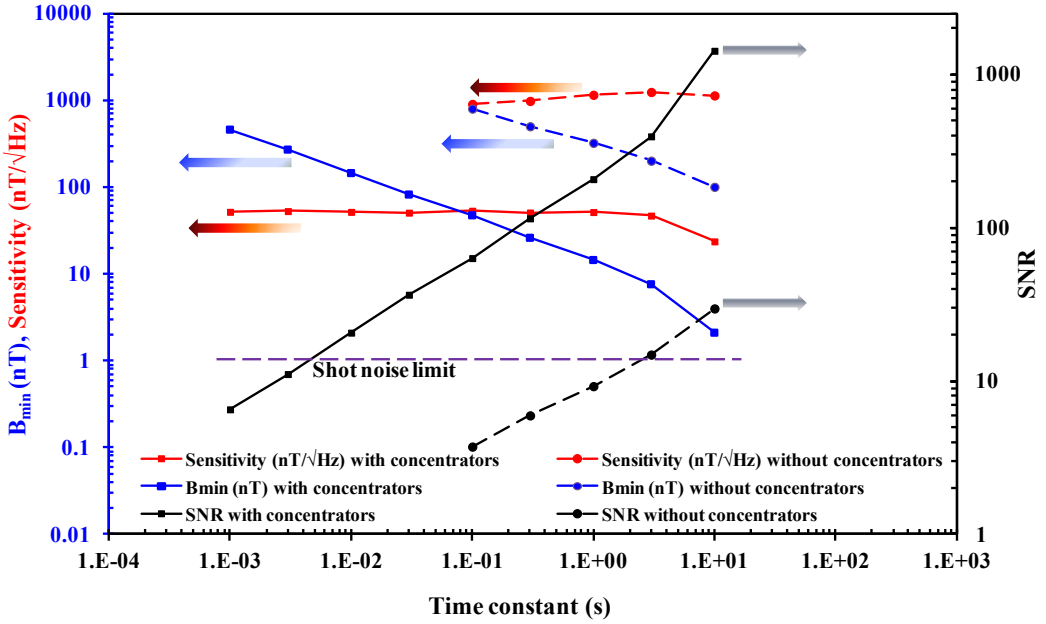

Figure 16. SNR, B_{min} and sensitivity of the magnetometer as a function of measurement time constants in the absence and presence of magnetic flux concentrators. Solid lines correspond to performance with concentrators and dashed lines correspond to performance without concentrators.

The shot noise limited minimum detectable field sensitivity B_{SN} of the sensor is influenced by the responsivity R of the detector, the saturation power P of the photoreceiver and the MO responsivity S, consisting of the product of the Verdet constant V and the thickness L of the film, according to (3) and (4), where e is the electron charge (1.602×10^{-19}C), R is 0.75A/W at 980nm, and P is 0.5×10^{-3}W.

$$B_{SN} = \frac{1}{S}\sqrt{\frac{e}{2RP}} \tag{3}$$

$$S = VL \tag{4}$$

The autobalanced noise cancellation from the photoreceiver and the two pass configuration, increase *S* by a factor of 200 and 2, respectively, in addition to the product of the Verdet constant and the film thickness to account for the MO response $S = 816°/T = 14.2$ rad/T. This corresponds to a shot noise limited minimum detectable field sensitivity $B_{SN} = 1$ nT/√Hz. This calculated shot noise limit is shown in Fig. 16, illustrating the enhancement of the sensitivity by using the magnetic field concentrators to reduce the gap above the shot noise limit. The relative frequency response was measured between 20Hz and 10kHz as shown in Fig. 17, and indicated the sensor bandwidth to be around 10kHz. The SNR as observed at 500Hz with the control field of 3μT was 41 dB (dB=20log(SNR)) and showed a 1/f noise trend at low frequencies as shown in Fig. 17 inset. The frequency response of the sensing system at lower frequencies is influenced by several factors such as the limitation of the autobalancing loop speed in the photoreceiver, the attenuation of the 60 Hz filter in the lock-in amplifier and the overall dominance of 1/f noise. The high frequency response of the sensing system is expected to be limited only by Helmholtz coil secondary effects rather than the nanocomposite frequency response. The field was measured using a Lakeshore Hall probe gaussmeter for frequencies below 600Hz, as well as magneto-optically using BK7 glass. Since BK7 is a diamagnetic material and therefore its MO response is independent of the modulating frequency, it can be used to calibrate the magnetic control field from 600Hz to 10kHz.

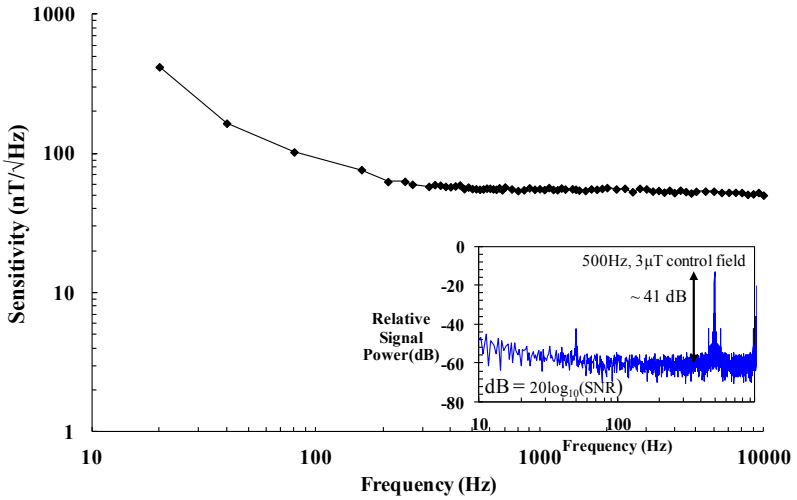

Figure 17. Relative frequency response of the $CoFe_2O_4$ based sensor. Inset: Fast Fourier transform of the magnetometer output signal waveform at 500Hz at 980 nm with a control magnetic field of 3μT.

Using a very similar $Co_xDy_{(1-x)}Fe_2O_4$ nanoparticle based polymer composite, an all fiber magnetic field sensor prototype has been developed with 1pT magnetic field sensitivity. Figure 18 shows the all-fiber prototype and magnetic field noise floor of the same using the above-mentioned composite as a sensing element. To summarize, novel methods of preparing nearly monodisperse cobalt ferrite, cobalt and magnetite nanoparticle-based polymer composites have been developed under this program. As a result of the low level of nanoparticle clustering and aggregation, the optical quality of the cobalt ferrite polymer nanocomposite shows an FOM of 0.95° at 980nm, comparable to YIG FOM of 4.2° at 980nm. In various composites reported here we have achieved FOM up to 3.8° at the same wavelength. A proof of principle all-optical magnetometer with a noise equivalent magnetic field sensitivity of 50 nT/√Hz and an all-fiber prototype with a 1pT magnetic noise floor indicates that these highly transparent and MO responsive materials may be used in magnetic field sensing systems where high sensitivity is required.

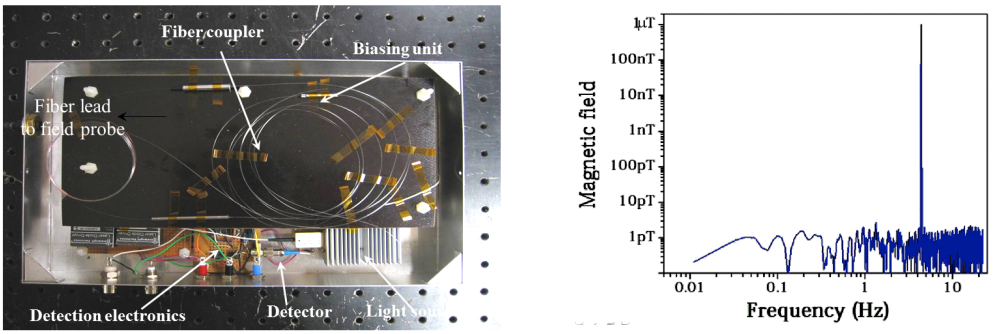

Figure 18. Left: All-fiber magnetic field sensor prototype, Right: 1pT magnetic field noise floor.

A fiber based prototype isolator: To demonstrate a prototype isolator and develop the necessary characterization facilities, we have developed a fiber-based prototype Faraday rotator that shows as much as 45° of nonreciprocal rotation under a 0.98T field. The prototype uses a 3.2cm long fiber (hereby designated FiberX1) and commercially obtained NdFeB magnets with small form factors. Detailed MO measurements on the fiber show potential for a true fiber based MO isolator using only ~ 4cm of fiber at 980 nm with a 1T applied field. The fiber under test FiberX1 was acquired from an outside source and has a core diameter of 4μm and an NA of 0.16. The FR experienced by light in an optical fiber is different from that shown in bulk material. In optical fiber, the core and cladding are made from different materials and hence exhibit different Verdet constants. Only a portion of the guided mode is confined within the core of the fiber waveguide and the effective Verdet constant, V_{eff}, is defined as the net Verdet constant experienced by the optical mode within the fiber,

$$V_{eff} = V_{core}\alpha + V_{cladding}(1-\alpha) \tag{5}$$

where in (5) V_{core} and $V_{cladding}$ are the Verdet constants of the core and cladding of FiberX1, respectively, and the confinement factor $\alpha = P_{core}/P_{total}$ is the ratio of the power contained in the core, P_{core} to the total power, P_{total}. The confinement factor can be approximated as α =1.306-1.138/ν based on the ν value of the fiber and according to Yoshino, et. al. (*J. Opt. Soc. Am. B*, **22**, 1856 (2005)) the Verdet constant in a fiber is strongly dependent on this ν value. It has also been suggested that the confinement factor can be as high as 0.8. Figure 19 describes our setup schematically and to obtain efficient coupling and maximum mode confinement a microscope objective with NA of ~ 0.2 or less was used as the input. No attempts were made to accurately measure the confinement factor and the measured Verdet constants are effective Verdet constants. Verdet constants were measured using an AC magnetic field and light at 850nm, 980nm, 1310nm and 1550nm, together with a novel autobalanced signal detection protocol (P. Gangopadhyay et. al., *J. Phys. Chem. C* **112**, 8032 (2008)). Linearly polarized light oriented at 45° to the horizontal plane from a Glan-Thomson polarizer (with extinction better than 56dB) was coupled to a 3.2cm test section of FiberX1 placed inside a solenoid. The AC magnetic field was generated using a broadband home-made amplifier cascaded with a SR830 lock-in amplifier; the frequency and magnitude of the magnetic field are controlled from the lock-in amplifier. Figure 20a shows the linear dependence of the magnitude of FR on the applied magnetic flux density at wavelengths 850nm, 980nm, 1305nm, and 1550nm. For comparison, we have also measured FR of a 3.2cm long SMF28 fiber at 1305nm. FiberX1 appears to have ~ 20 times larger FR than SMF28 at 1305nm, indicating promise for an all fiber MO isolator. The effective Verdet constant of FiberX1 has been calculated as $V_{eff} = \frac{1}{l} \times \frac{\partial \theta_F}{\partial B}$ where l is the length of the fiber under test (3.2cm), θ_F is the

measured FR and *B* the magnetic flux density. Figure 20b shows the wavelength dependence of the effective Verdet constant of FiberX1, where the solid line is a Cauchy fit to the data.

Table 5 lists the effective Verdet constants of FiberX1 at various wavelengths along with that of SMF28 at 1305 nm. Required lengths of FiberX1 to achieve 45° of rotation at various wavelengths with 1T of magnetic field are also listed in Table 5. Note that over the wavelength range of interest the sign of the effective Verdet constant of FiberX1 is negative and opposite to that of SMF28 indicating the presence of paramagnetic materials/ions as dopants in the fiber core. The effective Verdet constant of FiberX1 was found to be -1163°/Tm at the wavelength of interest, 980nm. The measured Verdet constant of -548°/Tm is about 18 times larger than that of silica-based SMF28 at 1305 nm and demonstrates the potential for a compact all-fiber Faraday isolator. Using these results we have constructed a prototype MO rotator with non-reciprocal rotation up to 20º at 0.5T magnetic field at 980nm.

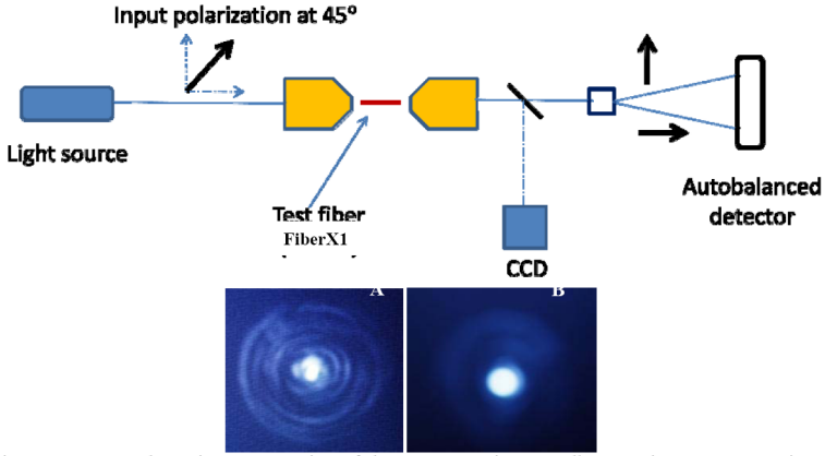

Figure 19. Top: Schematic representation of the setup, WP is a Wollaston prism. Bottom: A is an output profile from FiberX1 at 980nm and B is a profile captured at 1305nm

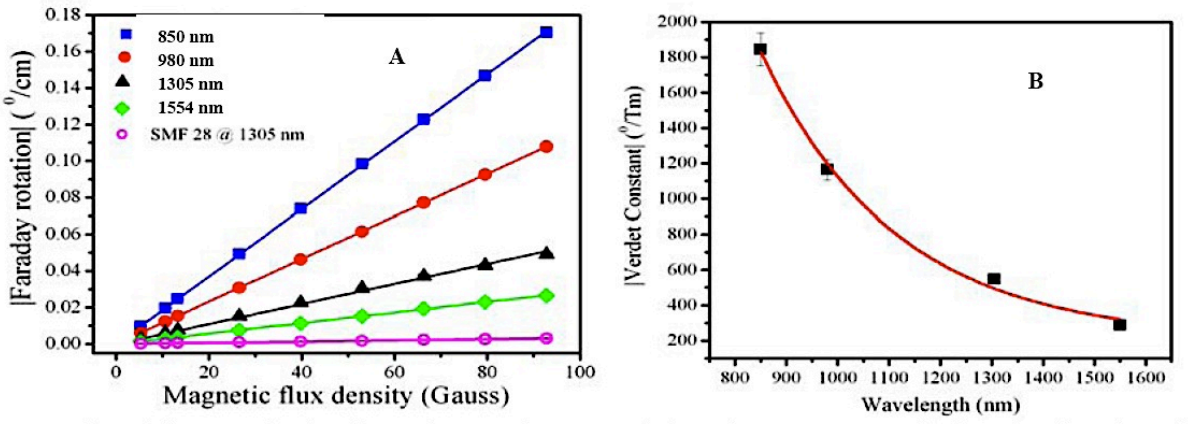

Figure 20. A. Plot of the magnitude of Faraday rotation per unit length versus magnetic flux density; the solid lines are linear fits with zero intercept. B. Wavelength dispersion of effective Verdet constant of FiberX1.

Table 5. *List of effective Verdet constants and required lengths to achieve 45° of rotation from FiberX1 at different wavelengths. Similar parameters for SMF28 were measured at 130 nm and are listed here for comparison.*

	V (°/Tm)	l (cm)
FiberX1 / 850 nm	- 1845	2.4 cm
FiberX1 / 980 nm	-1163	3.9 cm
FiberX1 / 1305 nm	- 548	8.2 cm
FiberX1 / 1550 nm	- 288	15.6 cm
SMF-28 / 1305 nm	+ 30	150 cm

Magnetic Ionic liquids: Magnetic room temperature ionic liquids (MRTILs) generally contain a paramagnetic metal ion and a soft organic cation combined with an appropriate anion to form a liquid salt. MO properties of these liquids are directly correlated to the metal ion susceptibility and its volume % in the liquid. MRTILs meet the requirements for construction of high power isolators and MO modulators. They can also be used as the MO transducer in a magnetic field sensor. Present day isolator technology primarily uses MO glasses or crystals as MO materials in laser isolators and generally they work in very narrow wavelength region. Commercially available MO isolator materials include glasses e.g. MR4, MR 3-2 and crystals e.g. terbium gallium garnet (TGG) and bismuth doped yttrium iron garnet (Bi:YIG) albeit highly absorbing in the wavelength region of technological importance. Thermal lensing and birefringence caused by such absorption makes these materials unsuitable in high power laser applications. We have synthesized a class of MRTILs with large Verdet constants that look promising for construction of liquid filled fiber isolators. Among these new liquids 1-decyl-3-methyl immidazolium gadolinium chloride ($[Dmim]_3GdCl_6$) is colorless and shows promise for a broadband isolator. These ionic salts are liquid at room temperature and are stable up to 350 °C; a high viscosity and relatively high refractive indices make MRTILs ideal candidates for further studies for construction of MO isolators usable within a large wavelength region.

Fig. 21 shows the optical properties of the MRTILs. Ionic salts prepared with $GdCl_6$ and Bmim were solid at room temperature and Dmim was used instead to take the melting point of the salt down to 12°C. MRTIL1, prepared with Gd^{+3} ions, is optically transparent and almost colorless within a broad range of wavelengths, from 400nm up to 1350nm. Absorption around 1550nm are most likely due to a large volume fraction of organic ion arising from the –CH bonds within the side groups; the –CH bonds in the side chains could be replaced with –CF to shift the absorption band away from the 1550nm region and will be pursued in future work. MRTILs are $A_mB_nX_p$ salts where A is the organic ion, B the metal ion and X the anion, generally being either halides, sulfates or phosphates. This composition of matter allows us to tune the volume magnetization (using different metal ions), concentration of metal ions, viscosity and melting point (using different organic cations), and optical properties (by changing metal ions and counter anions). Note that among these five, only MRTIL5 ($BmimFeCl_4$) has been reported before by others, but MRTIL1 – 4 are entirely new and represent a new class of MO materials with tunable MO and optical properties.

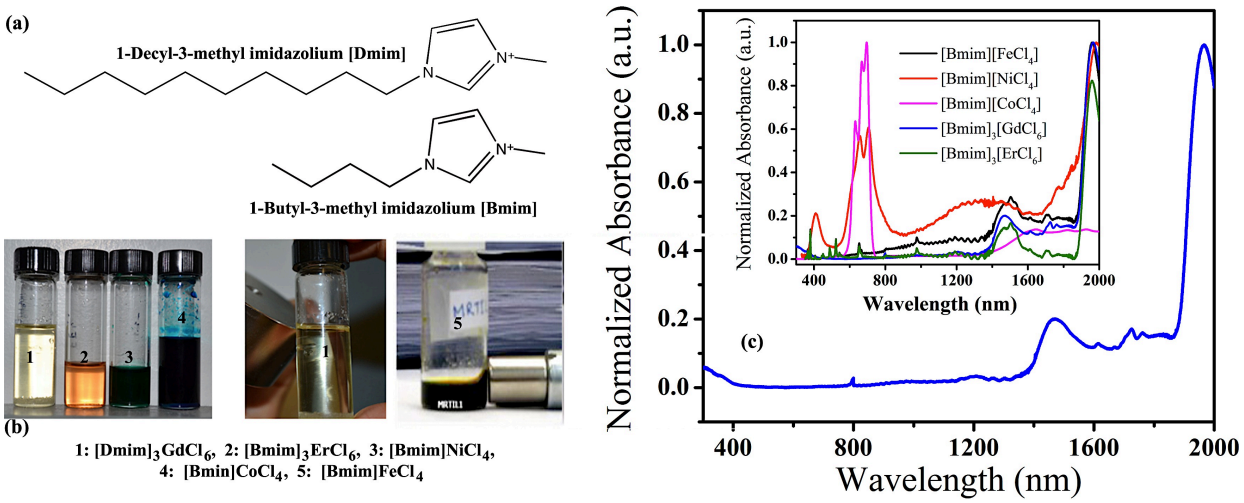

Figure 21. Optical transparency: (a) Molecular structure of the organic part of the ionic liquids, (b) photographs of various MRTILs studied in order of increasing absorption energy from left to right; also shown is their attraction to a magnet, (c) normalized (against the maximum absorption) absorbance spectra of all the liquids.

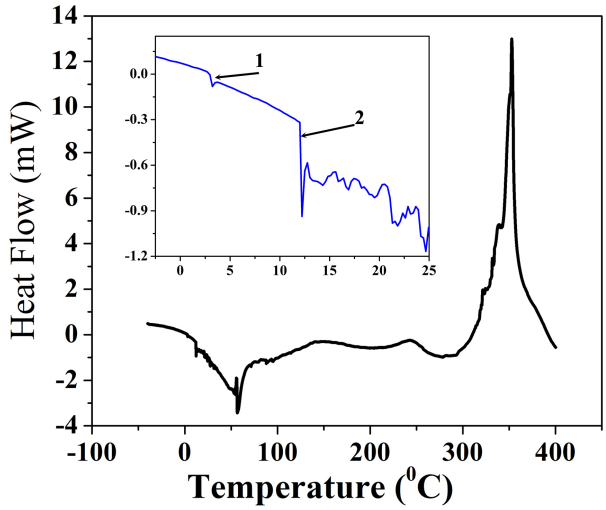

Figure 22. Thermal properties: Heat flow measured vs. temperature using a differential scanning calorimeter (DSC); points marked as 1 and 2 indicate respective phase changes at 4°C from water and at 12.5°C from $Dmim_3GdCl_6$ melting.

Fig. 22 shows a plot of heat flow within $[Dmim]_3GdCl_6$ against temperature measured using a differential scanning calorimeter (DSC). Point 1 in the plot indicates crystallization of water at ~ 3 – 4°C, a small amount of water is always present in these materials. $[Dmim]_3GdCl_6$ starts crystallization at or below 12.5°C and is liquid at room temperature. Decomposition of the liquid starts at ~ 300°C indicating thermal stability over a large temperature range. Note that crystallization is an exothermic process and appears as a dip in the DSC heat flow plot, while the reverse is true for decomposition, melting and boiling points. The dip at ~65°C is the crystallization point for DmimCl and indicates free organic components that are not attached to the metal. Further purification is currently being carried out to remove the unreacted organic part. DSC measurements done on the other MRTILs shows quiet similar

thermal stability (up to 300°C) with a sub-zero crystallization temperature for the Bmim based MRTILs; this is expected as at shorter side chain length the MRTILs are expected to have lower melting points.

Extensive EDAX / EDS spectroscopy measurements were carried out to verify the composition of the liquids. A thin liquid film was prepared using the doctor blading technique on a Si wafer; Fig. 23a shows an SEM image of a portion of this film. The same portion was mapped for Gd, Cl and Si, with the respective maps shown in Fig. 23 (b) – (d). The Gd and Cl maps indicate a homogeneous distribution of Gd and Cl within the liquid and a higher concentration of Cl as expected since there are 6x higher atomic concentrations than that of Gd. The EDS spectra clearly shows the absence of any other metals or impurities, indicating that the MO effects and magnetic susceptibility arise only from the Gd ions in the liquid; similar EDS studies in other MRTILs confirmed respective compositions. Along with EDS spectra, micro-Raman spectroscopy was done on the same portion of the liquid. The Raman spectra show that the MRTILs are a composite of metal ions, organic portion and chloride ions, indicating co-existence of the organic ions within the liquids. A composite micro-Raman spectra collected from MRTILs is shown in Fig. 24. A 514nm Ar^{+} laser integrated with the SEM used to collect the EDS spectra was used as excitation source for the Raman spectra. Er^{+3} based compounds are known for their fluorescence when excited with 514nm and a broad background fluorescence is seen in the Raman spectrum collected from MRTIL containing Er^{+3} ions (MRTIL2).

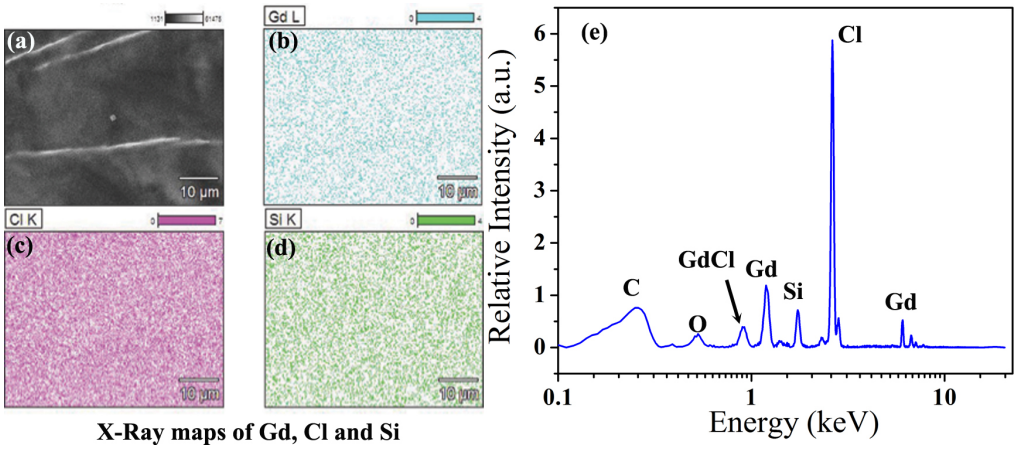

Figure 23. Composition analysis: (a) SEM image of the $[Dmim]_3GdCl_6$ film on Si wafer, (b) – (d) X-Ray maps of Gd, Cl and Si (from the substrate), (e) EDS spectra of $[Dmim]_3GdCl_6$

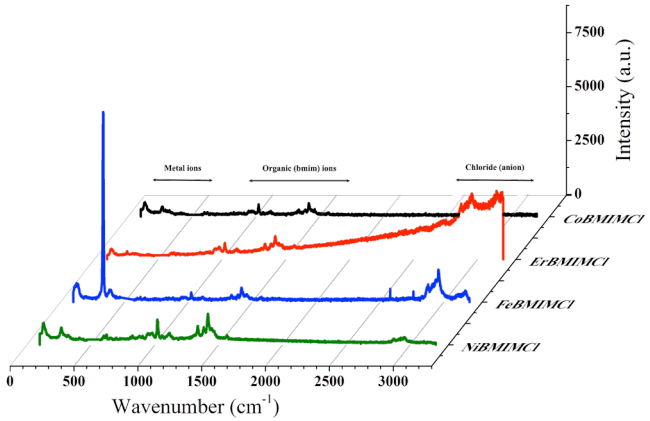

Figure 24. Composite Raman spectra of MRTIL2 – MRTIL5, frequency zones arising from different components of the liquid are indicated.

Table 6. Comparison of Verdet constant values at 980nm of two separate MILs with common materials; the values show potential of these MILs as MO candidate materials.

	V, Verdet Constant, @ 980 nm, ° / (Tm)
[bmim]$FeCl_4$	900
[dmim]$_3$$GdCl_6$	3024
BK7	106
p-Xylene	52
TGG	3420

The Verdet constant (see Table 6) of [bmim]$FeCl_4$ at 980 nm is ~ 9 times that of BK7 glass, whereas that of [dmim]$_3$$GdCl_6$ is ~ 30 times, close to commercially used isolator material TGG. Applying a typical magnetic field of 1 Tesla, these liquids can be used to build a 1 - 5 cm long isolator operating at 980 nm. The absorption spectra clearly show an available working window within the 400 nm to 1550 nm range. The Verdet constant in paramagnetic material can be correlated to its susceptibility according to the relation in (6).

$$V = \frac{2\pi}{\lambda^2} \times \frac{\chi_m}{g\beta h} \sum_{ij} \frac{C_{ij}}{\omega_0^2 - \omega_{ij}^2} \qquad (6)$$

where χ_m is the susceptibility at room temperature, λ the wavelength of interest, β is the Bohr magneton, ω_0 absorption maxima, C_{ij} and ω_{ij} are measures of the transition probability and energy splitting between the ground and excited states, respectively. For high power applications, optical absorption needs to be minimized which can be an important factor in the choice of the metal ion. Although magnetism in molecular materials is additive in nature, in ionic salts, the susceptibility will be mainly dependent on the metal ions in the paramagnetic state and the organic cation will primarily be responsible for the physical state of the salt, in particular, physical state, viscosity and thermal properties etc. The length of the alkyl side chain attached to the cation can be used to adjust the melting point of the salt.

We have been focused on developing an in-fiber isolator working within the wavelength range of 400 nm – 1350nm. An isolator working at 980nm and able to handle high laser powers could be beneficial for many applications. One of the advantages of liquid filled capillary fiber isolators is that the liquid can be circulated within the capillary as a method for self-cooling and self-healing. Figure 25 shows the experimental geometry of a representative liquid filled capillary fiber device. A 3.9cm long capillary fiber with 10μm inner diameter was used to fill in Gd^{+3} based ionic liquid via capillary suction; the MO studies are performed either by a free space – capillary fiber – free space geometry or a SMF28 can be spliced together with the capillary fiber to construct the isolator device. Interestingly, Gd^{+3} being a paramagnetic species, this liquid filled capillary fiber can be treated very similar to Tb^{+3} doped glasses that have been traditionally used for glass based fiber and free space isolator applications as discussed above. Paramagnetism arises from the non-zero angular momentum of the individual dopants (Gd^{+3}, $J \neq 0$), caused by the presence of unpaired electrons in the atomic orbitals. The resulting magnetization *M* is then given by $M = Ng\mu_B JB_J(\xi)$ where *N* is the number density of dopant atoms, *g* the Landé splitting factor, μ_B the Bohr magneton, B_J the Brillouin function, *J* the total orbital quantum number. At room

temperature, the Brillouin function can be expanded in a Taylor series and the paramagnetic susceptibility approximated as $\chi_p = \frac{NJ(J+1)g^2\mu_B^2}{3k_BT}$, where k_B is Boltzmann's constant and T is the temperature in Kelvin. The effective Verdet constant can then be expressed as the sum of diamagnetic and paramagnetic contributions $V_B = V_B^{dia} + V_B^{para} = V_B^{dia} + A\frac{NJ(J+1)g^2\mu_B^2}{3k_BT} = V_B^{dia} + \frac{C}{T}$, where V_B^{dia} depends on the organic part of the ionic liquid and is expected to be small, with A and C material constants. Generally V_B^{dia} and C have opposite sign with C having a much larger magnitude. However, the relationship shows that the FR and hence the isolation performance in the isolator will be highly temperature dependent and may become a bottleneck in high power laser applications. To avoid temperature build up the liquid must be percolated continuously to avoid degradation of isolator performance and/or the materials damage. An inverse relationship with temperature also indicates that these materials can be readily used for low temperature high performance applications. Below 8°C Gd^{+3} ionic liquid becomes semi-crystalline solid and will require additional performance analysis; although the phase stability at higher temperature is significantly high and is stable up to 670° C.

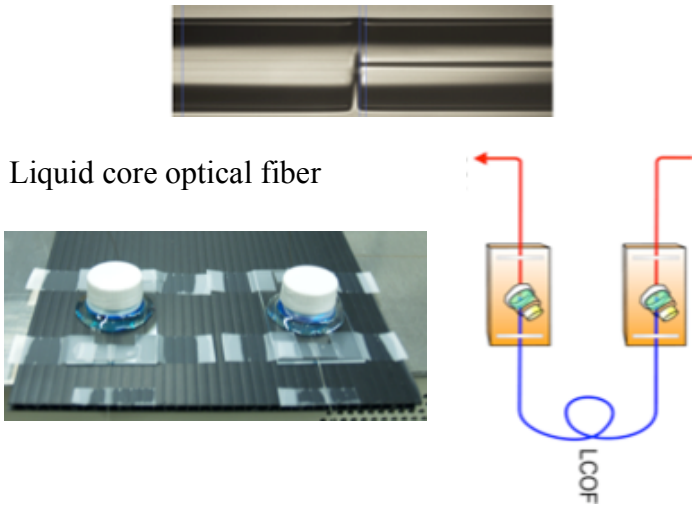

Figure 25. Schematics and photograph of representative liquid core optical fiber, a similar one was used for the MO Faraday rotation measurements reported here.

However, long device length also adds to the complexity of predicting FR performance based on the Verdet constant, particularly due to inhomogeneity of the magnetic field over such long lengths. A geometrical factor must be added to accommodate the magnetic permeability and magnetic field variation and can be expressed as: $V_B = \frac{\theta_F}{\mu K_G}$ where μ is the magnetic permeability of the material and K_G is the geometric factor. The geometric factor, K_G is dependent on the relative ratio of the optical length and magnetic field length that can be expressed as $K_G(L_M, L) = \left(\sqrt{(L_M^2 + L^2) + 4R^2} + \sqrt{(L_M^2 - L^2) + 4R^2}\right) / 2L_M$, where L_M is the length of the magnet, L is the length of the fiber and R is the radius of the magnet. In the device K_G must have a value of 1 to be able to extract maximum leverage from the Faraday rotation. Figure 26 shows the isolation data from the first proof of concept isolator device.

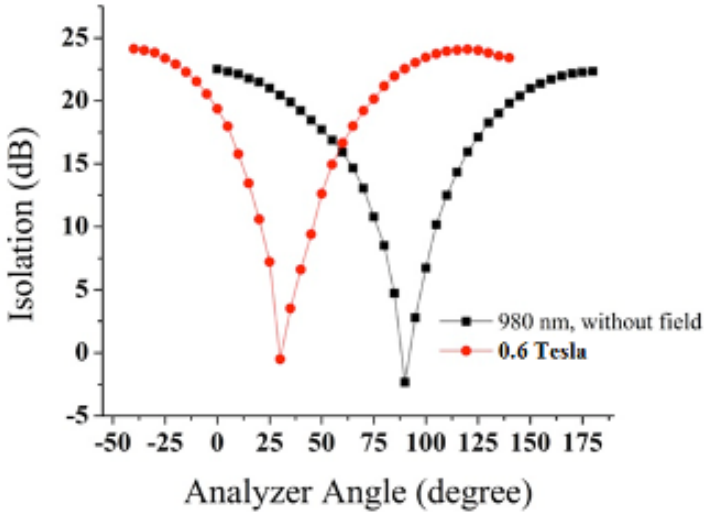

Figure 26. Measured isolation at various analyzer angles at 980nm from 3.9cm long capillary fiber filled with Gd^{+3} based magnetic ionic liquid.